AFRL-AFOSR-VA-TR-2024-0233

Controlling damage mechanisms in metamaterial composites with multiscale interfaces

Matlack, Kathryn
UNIVERSITY OF ILLINOIS
506 S WRIGHT ST
URBANA, IL, 61801
USA

05/30/2024
Final Technical Report

Air Force Research Laboratory
Air Force Office of Scientific Research
Arlington, Virginia 22203
Air Force Materiel Command

REPORT DOCUMENTATION PAGE

PLEASE DO NOT RETURN YOUR FORM TO THE ABOVE ORGANIZATION.

1. REPORT DATE	2. REPORT TYPE	3. DATES COVERED	
20240530	Final	START DATE 20200128	END DATE 20240128

4. TITLE AND SUBTITLE
Controlling damage mechanisms in metamaterial composites with multiscale interfaces

5a. CONTRACT NUMBER	5b. GRANT NUMBER	5c. PROGRAM ELEMENT NUMBER
	FA9550-20-1-0036	61102F
5d. PROJECT NUMBER	**5e. TASK NUMBER**	**5f. WORK UNIT NUMBER**

6. AUTHOR(S)
Kathryn Matlack

7. PERFORMING ORGANIZATION NAME(S) AND ADDRESS(ES)
UNIVERSITY OF ILLINOIS
506 S WRIGHT ST
URBANA, IL 61801
USA

8. PERFORMING ORGANIZATION REPORT NUMBER

9. SPONSORING/MONITORING AGENCY NAME(S) AND ADDRESS(ES)	10. SPONSOR/MONITOR'S ACRONYM(S)	11. SPONSOR/MONITOR'S REPORT NUMBER(S)
Air Force Office of Scientific Research 875 N. Randolph St. Room 3112 Arlington, VA 22203	AFRL/AFOSR RTA1	AFRL-AFOSR-VA-TR-2024-0233

12. DISTRIBUTION/AVAILABILITY STATEMENT
A Distribution Unlimited: PB Public Release

13. SUPPLEMENTARY NOTES

14. ABSTRACT
The goal of the proposed research is to develop metamaterial composites that control damage, using magneto-active elastomers and the design of the composite's geometry. While polymer matrix composites are well known for their high stiffness, lightweight, and high strength mechanical properties, they typically suffer from subpar fracture toughness, are prone to damaging vibrations, and have no mechanism to adapt their properties in the presence of a propagating crack. The proposed work addresses these limitations of traditional composites, by engineering weak interfaces, the stiffness of which can be tuned with an applied magnetic field, in specific architectures in polymer matrix composites. Our hypotheses are that interfaces in engineered composites at different length scales control damage in composites, tunable stiffness materials can change the fracture toughness and crack propagation path of the composite through actuations, and resonant and periodic features combined with friction at interfaces in composites will mitigate damaging vibrations and enhance mechanical dissipation. The technical approach of the proposed work is to systematically study multi-scale interfaces in metamaterial composites to understand their role in controlling crack propagation. We will use advanced direct ink write methods to fabricate the metamaterial composites in complex geometries with tunable stiffness interfaces. We will experimentally characterize the mechanical properties, vibration responses, and crack propagation from micro to macro scales, and study how these properties can be controlled with magnetic actuations. We will predict the coupled magneto-mechanical-vibration properties using experimentallyinformed analytical and finite element method models of the developed composites. The anticipated outcomes are new composite materials that have enhanced fracture toughness, can redirect crack propagation, and mitigate damaging vibrations. The potential impact of this research is advanced lightweight structural components with engineered mechanical properties (fracture toughness, strength, and vibration mitigation) for USAF-related applications.

15. SUBJECT TERMS

16. SECURITY CLASSIFICATION OF:			17. LIMITATION OF ABSTRACT	18. NUMBER OF PAGES
a. REPORT U	b. ABSTRACT U	c. THIS PAGE U	UU	30

19a. NAME OF RESPONSIBLE PERSON	19b. PHONE NUMBER *(Include area code)*
GREGG ABATE	

Section 2: Final Technical Report

Accomplishments

- ***Research Objectives:***

The overall goal of this project is to understand how to control damage mechanisms in composites with metamaterials. The specific research objectives were:

(1) Determine how interfaces at multiple length scales influence mechanical properties, crack propagation and vibration and dissipation properties of smart composites.

(2) Characterize how smart metamaterials adapt their fracture toughness and crack propagation properties.

(3) Understand the role of mechanical band gaps on fracture toughness and crack propagation.

- ***Please provide details of accomplishments during this reporting period.***

Major activities	**Specific objective addressed**	**Significant results**
1. Fabrication of smart composites, including magneto-active elastomers (MAEs), vitrimer epoxy, MAE-aluminum composites, and metal matrix composites	Develop fabrication approaches realize magneto-active smart materials to address overall objectives (1) and (2)	1. A repeatable fabrication approach was identified for MAEs, including anisotropic specimen with different weight percentages of CIPs. 2. Vitrimer epoxy was not successful using direct ink write, since the cure time was faster than the fabrication process. 3. A fabrication approach was developed for aluminum-MAE composites, with a PDMS that preferentially bonds to aluminum. This approach is promising for fracture studies in composites. 4. A new class of metal matrix composites comprised of stainless steel and bronze were developed by modifying the binder jet 3D printing process to obtain a prescribed spatial distribution of constituent materials.
2. Experimental characterization of smart composites (vitrimer epoxy, MAEs) from micro- to macro-scales: mechanical testing, scanning electron microscopy, and optical microscopy	Determine how interfaces at multiple length scales influence mechanical properties, crack propagation and vibration and dissipation properties of smart composites.	1. Dynamic magneto-mechanical analysis testing characterized the storage and loss modulus in MAEs as a function of particle loading, strain amplitude, frequency, and magnetic field. 2. Mechanical testing of MAEs showed an increase in fracture toughness in these composites compared to neat PDMS, 3. Scanning electron microscopy identified various toughening mechanisms characteristic of particulate composites. 4. Anisotropy in MAEs can change the directional fracture toughness by up to 1.5 times. 5. Fracture tests and SEM imaging explains the micromechanics of how internal geometry, including the existence of waviness in the

		particle chain, the distance between chains and particles, and the type of chain alignment, can each individually affect the fracture behavior of anisotropic MAEs. 6. Optical microscopy revealed the spatial distributions in stainless steel-bronze MMCs from the modified binder jet process. 7. Mechanical testing of vitrimer epoxy samples showed very large variation in mechanical properties, that would be prohibitive to use in these smart composite studies. 8. Lap shear testing of vitrimer epoxy and PDMS showed a relatively weak bond at the interface. 9. Mechanical testing of aluminum-PDMS bond strength showed that fracture occurred in the PDMS, indicating a relatively strong bond. 10. Initial fracture tests of MMCs showed that binder jet 3D printing can be used to modify the fracture properties and control crack propagation in stainless steel-bronze composites.
3. Experimental characterization of controllable crack propagation in smart composites	Characterize how smart metamaterials adapt their fracture toughness and crack propagation properties.	1. An applied magnetic field of 0.3T caused an increase of fracture toughness in anisotropic MAEs with 35% vol fraction of carbonyl iron particles, through crack tip shielding. 2. Other MAE anisotropies and volume fractions did not exihibit an influence of magnetic field on crack propagation and fracture toughness.
4. Finite element modeling of crack propagation in MAEs, including multi-physics modeling of their coupled magneto-mechanical properties,	Determine how interfaces at multiple length scales influence mechanical properties, crack propagation and vibration and dissipation properties of smart composites. Characterize how smart metamaterials adapt their fracture toughness and crack propagation properties.	1. Finite element models that incorporate a phase field approach to characterizing crack propagation were developed, and initial simulations showed that cracks in MAEs will deviate their path at an angle that is related to the strength of the magnetic field. These promising results give us a mechanism with which to tune crack propagation, based on magnetostriction in the MAE.

5. 2D benchmark simulations employing Phase Field-Cohesive Zone Model (PF-CZM), offer insights into crack propagation in MAEs with different CIP distributions and volume fractions.	Determine how interfaces at multiple length scales influence mechanical properties, crack propagation and vibration and dissipation properties of smart composites. Characterize how smart metamaterials adapt their fracture toughness and crack propagation properties.	1. Model results reveal that the increase in fracture toughness in high volume fraction anisotropic MAEs is likely due to an increase in crack propagation path from wavy chains in the MAE microstructure.
6. Developed a computational homogenization approach to analyzing the magneto-mechanical coupling in anisotropic magneto-active elastomers.	Determine how interfaces at multiple length scales influence mechanical properties, crack propagation and vibration and dissipation properties of smart composites.	1. A computational homogenization approach revealed that the magneto-mechanical coupling in magneto-active elastomers is primarily driven by the straightness of particle chains and the spacing between particles in the matrix. 2. These results constitute a toolbox for design of anisotropic magnetostrictive devices which can be readily integrated into numerical optimization routines, with the microstructural parameters such as volume fraction and chain direction as design variables.
7. Characterized the effect of high viscoelasticity on band gaps in MAEs.	Understand the role of mechanical band gaps on fracture toughness and crack propagation.	1. The concept of "fuzzy band gaps" was introduced as an experimentally-informed measure of spatial attenuation viscoelastic phononic crystals. This is a first step toward understanding how damped band gaps might relate to fracture toughness in smart materials.

- ***How were the results disseminated to communities of interest? If there is nothing significant to report during this reporting period, state "Nothing to Report."***

Research results were disseminated to the research community through two journal publications thus far,

a Ph.D. thesis, three journal publications under review, and several conference presentations including invited talks (US NC-TAM, Society of Engineering Sciences) and seminars (Brown University, UC San Diego, UIUC, Lawrence Livermore National Lab, and the International Committee on Jointed Structures) given by the PI. Results were also disseminated to AFRL through informal collaboration meetings with AFRL participants.

Impacts

Development of the principal discipline(s) of the project

The numerical and experimental results suggest that magnetic fields can be used to change the fracture toughness and direction that cracks propagate in smart composites, which is a new contribution to the field of mechanics and materials. We also developed a new homogenization modeling approach that uses coupled multi-physics simulations to understand the origins of magneto-mechanical coupling in magneto-active elastomers. These results may have broad-reaching applications in understanding mechanical properties and damage mechanisms in stimuli-responsive materials in general.

Other disciplines:

The materials developed and experimental results may influence the field of fracture characterization in soft materials. The proposed fracture tests in this work use magnetostriction to induce mixed mode fracture in an MAE; experimentally characterizing fracture under mixed modes is typically extremely difficult in practice. Using applied magnetic fields and a composite material composed of a region of an MAE and a separate region of the pure elastomer that comprises the MAE may allow researchers to experimentally study mixed mode fracture in elastomers.

Describe the impact in this reporting period on the development of human resources

This project included mentoring a total of 4 graduate students, each of whom developed new research skill sets during the project, and were mentored on conducting research, analyzing data, and scientific communication. All students gained experience presenting their research to and collaborating with AFRL researchers. One student traveled to AFRL and worked directly with the AFRL collaborators for several days. One student who was supported by this grant and an NDSEG fellowship completed his Ph.D. degree during the project (December 2023), and his thesis was directly on this project.

Describe the impact on teaching and educational experiences

This project was used in course materials for TAM 451: Intermediate Solid Mechanics, taught by the PI in Fall 2021 and 2023 at UIUC. Activities and results from this project were used as examples of new materials to control fracture and complexities in experimental fracture mechanics, especially in the context of composites. This course is tailored to advanced undergraduate students in the Engineering Mechanics major at UIUC, as well as graduate students in solid mechanics.

Describe the impact in this reporting period on physical, institutional, and information resources that form infrastructure.

Activities during this project included the development of multiple new laboratory facilities to study the magneto-mechanical coupling in MAEs and MAE composites. A custom dynamic mechanical analysis measurement setup was modified to study the magnetic field dependence of the storage and loss modulus in MAEs along different orientations and over a broad range of frequencies, up to 1kHz. Several custom

fracture measurement setups were constructed to characterize crack propagation in MAEs and MAE composites, and to probe the influence of an external magnetic field on fracture in MAEs.

Impact on society beyond science and technology:

n/a

Changes

Changes in approach

There was a minor change in our material platform for the composites. Since mechanical properties of the vitrimer epoxy were very inconsistent and much lower than anticipated, we are now working with different composites ranging from metal matrix composites, and aluminum/magneto-active elastomer composites. We have identified an elastomer that is a PDMS that preferentially bonds to aluminum, such that all the scientific questions posed in the original project can still be pursued. This change is somewhat related to COVID, since we originally planned significant travel to work with AFRL collaborators, who had developed the vitrimer material. This travel was significantly delayed and reduced due to COVID.

Problems or delays

As reported above, the inconsistent mechanical properties of the vitrimer epoxy imposed some problems to our material platform, so we have shifted this component of the composite to aluminum combined with a specific PDMS (Dowsil SE1700 PDMS) that preferentially bonds to aluminum. This resolved the issue, however this plus the delays from COVID prompted the NCE to be sought for 2023-2024.

Expenditure Impacts

COVID prevented some travel funds to be used as a means to access facilities at AFRL for experiments. We shifted these funds to facility fees at UIUC.

Significant changes in the use or care of human subjects, vertebrate animals and/or biohazards

n/a

Changes to the primary place of performance from that originally proposed

n/a

Technical Updates

1. Task 1: Fabrication, characterization, and evaluation of smart magneto-active elastomer (MAE) composites

1.1 Development and fabrication of PMC material

To realize the PMC-MAE metamaterial designs, we sought a stiff polymer that would readily adhere to an MAE material. The Air Force Research Laboratory had developed an epoxy which showed potential to bond well with PDMS, due to dynamic covalent bonding. AFRL provided the base material of the epoxy (KPAMS) to UIUC, where we mixed it with Bisphenol A diglycidyl ether (DGEBA) and cured it in tensile specimens. The samples fabricated at UIUC were an order of magnitude lower stiffness than those fabricated at AFRL. UIUC Graduate student E. Smith traveled to AFRL to work with AFRL chemists to fabricate samples and determine what was causing the discrepancies in stiffness. The samples the student fabricated at AFRL were qualitatively similar stiffness to the samples fabricated by AFRL personnel, but the samples were unable to be removed from the mold for quantitative testing. (AFRL molded smaller tensile specimens that were able to be removed from the mold). Specimens were again fabricated at UIUC using a new mold that facilitated the removal of the specimens, but the specimens fabricated at UIUC were never as stiff as those fabricated at AFRL. For 18 samples tested from three separate batches of KPAMS from AFRL, the modulus values ranged from 4 to 410 MPa, with an average modulus of 123 MPa. This large variation in properties could be due to KPAMS batch, age of KPAMS, changes in the KPAMS during shipping, influence of the size of the sample, or another factor.

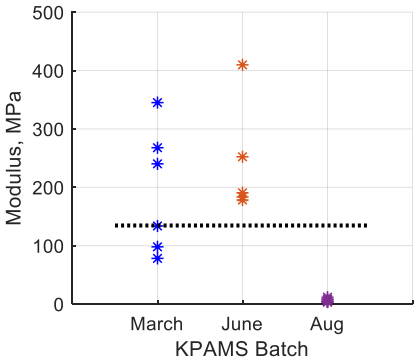

Figure 1. Modulus values for pure epoxy. Dotted line represents the average value across all batches.

To characterize the bond between MAE and epoxy, we fabricated and tested lap shear samples. The maximum lap shear strength recorded in the specimens (0.175 MPa) is similar to or below shear lap-shear adhesion values reported of PDMS bonding to metals. Because the epoxy did not show a significant improvement in adhesion strength compared to other materials, and we were unable to fabricate epoxy with consistent material properties at UIUC, we decided to pursue other materials and approaches to fabricate the metamaterials.

Using the direct ink write approach to fabricating a printable formulation of the epoxy (section 1.2), we performed tensile tests on the nanoclay-epoxy material and found that the average modulus was 585 MPa, which is greater than the pure epoxy samples. We printed a tensile specimen on the HYREL machine, but there were large spaces between the paths of vitrimer. Even with these large spaces, the modulus of the printed sample fell at the low range of values in the molded samples.

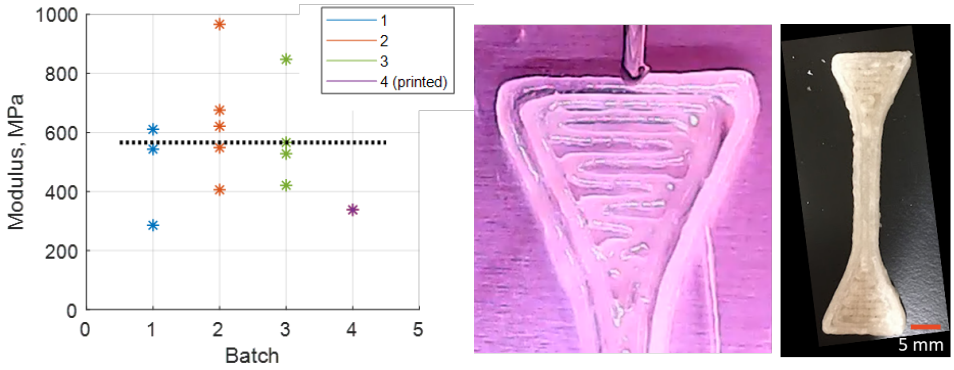

Figure 2. Modulus values for nanoclay-epoxy (left). Batches 1-3 are molded and batch 4 is printed. Printing of epoxy (center). Cured printed tensile sample (right)

1.2 Direct-ink Write Additive Manufacturing of Vitrimer-Nanoclay Composites

To enable fabrication of architected geometries for magnetically-tunable crack control, we first developed a direct-ink write (DIW) additive manufacturing process for vitrimer-based materials. Vitrimer (KPAMS-DGEBA epoxy) was prepared using a bladeless mixer and a small amount of nanoclay platelets were added to give the requisite rheological properties for DIW 3D printing. The material was then transferred to a syringe from which it was extruded through a nozzle on a commercial 3D printer (HyRel 3D System 30M) as shown in Figure 4. These experiments showed that the vitrimer-nanoclay material system was not a good candidate for DIW additive manufacturing, as the rapid cure rate of the vitrimer allowed only 15-45 minutes of printing, which was insufficient to produce anything but simple geometries of very small volume (less than 5 mL).

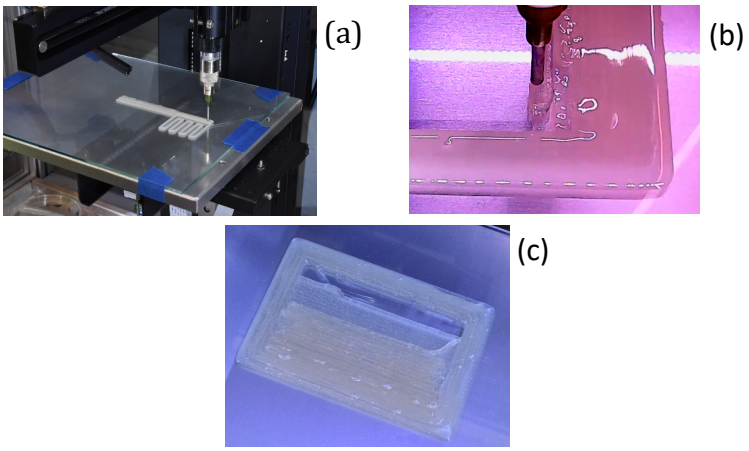

Figure 4: (a) 3D printer setup for vitrimer direct-ink writing. (b) Direct-ink write nozzle dispensing vitrimer. (c) Failed test print. The vitrimer cured and solidified in the dispense system before the print could be completed.

1.3 Fabrication of anisotropic soft MAEs (sMAEs)

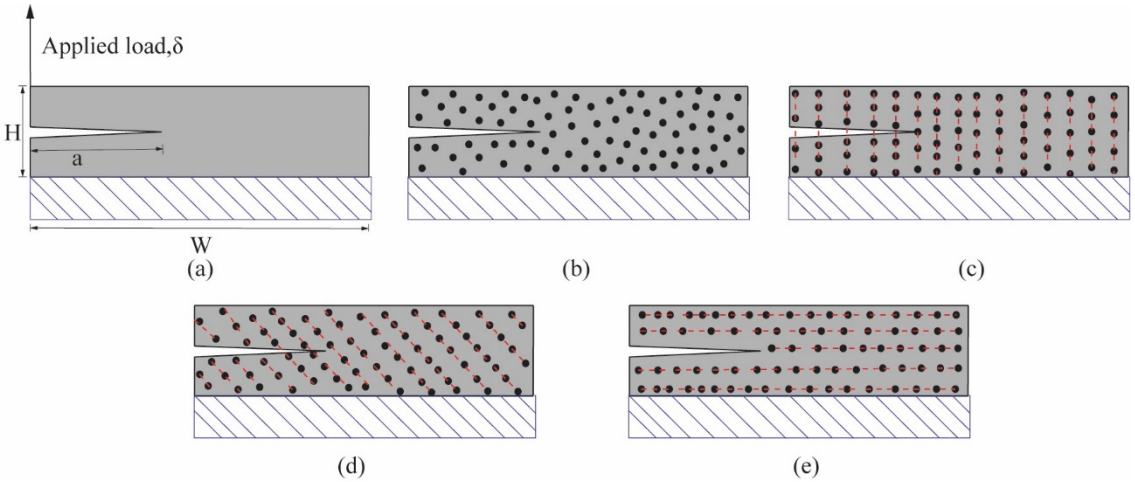

Figure 5 Pre-cracked specimens for fracture toughness testing. (a) PDMS, (b) isotropic sMAE, (c) anisotropic 0° sMAE, (d) anisotropic 45° sMAE, and (e) anisotropic 90° sMAE. Hashed lines denote fixed support.

To study influence of multiscale features on crack propagation in smart composites, soft magneto-active elastomers were chosen as the material platform. These materials contain metallic ferromagnetic (i.e. "soft" magnetic) particles that do not hold a remnant magnetic field, embedded in a mechanically soft matrix. These particles can be isotropically distributed throughout the soft matrix (e.g. Fig 5b), or aligned in chain geometries (e.g. Fig 5c-e) by curing the material in the presence of a magnetic field. Here, we studied the influence of these directional chains on fracture properties, given the multiscale nature of the composite: the interface between the metal particles and soft matrix, the soft matrix properties, and the alignment of the particles.

The sMAEs were fabricated by combining PDMS (Dow Sylgard 184) and carbonyl iron particles (CIP) (US Research Nanomaterials, Inc.). The particles have soft magnetic properties, i.e. they have zero magnetization in the absence of an externally applied magnetic field, are approximately spherical in shape, and have an average particle diameter of 3 μm. The sMAE samples were fabricated by mixing CIPs into the elastomer at volume fractions ranging from 0% to 35% as listed in Table 1. sMAE samples were named based on their volume ratio; for example, sMAE06 designates a sample with a 6% filler in the matrix. To fabricate isotropic sMAEs, the prepared mixture was cured at 70◦C for 105 minutes without applying an external magnetic field which ensured a random distribution of CIPs in the matrix. To fabricate anisotropic sMAEs, the mixture in the mold was cured under an external magnetic field with a flux density of ∼0.2 T, which resulted in particle chains that were aligned with the magnetic field and depended on the orientation of the magnets with respect to the mold. Samples were fabricated with chains aligned at 0◦, 45◦, and 90◦ with respect to the direction of applied load in the fracture measurements. The detailed configurations of all the tested samples are illustrated in Figure 5. The fracture energy of each specimen was determined using the Rivlin and Thomas method[1]. The DIC software Vic-2D was used to analyze the images and detect the crack propagation onset point on the load-displacement curves. The following formula was used to determine the energy absorption during fracture:

$$G_c = \frac{A(\lambda_c)}{Wt}$$

Where $A(\lambda_c)$ is the elastically stored energy per unit volume required to initiate fracture, W and t are the sample width and thickness, respectively. The post-fractured surface was coated with Au-Pd and then scanning electron microscopy (SEM) (JEOL 7000F) images were obtained to understand the micromechanics that control the fracture properties.

Table 1: Categories of fabricated MAEs

Sample	Volume fraction (% of CIP)
PDMS	0
sMAE06	6
sMAE12	12
sMAE21	21
sMAE29	29
sMAE35	35

1.4 Introduce fabrication method for phase fraction control of constituent materials in binder jet printed Metal Matrix Composites (MMCs)

In the standard binder jet printing process, binder is selectively deposited in the regions where the designed part is defined. After printing, the part resides on the print bed and is surrounded by loose powder from the regions where no binder was applied. The part then undergoes a curing step, where the binder is cured. Before the final high-temperature sintering step, the part is depowered, i.e., the loose powder is completely removed from the part. Our new fabrication process simply modifies the CAD model such that a region of cavity containing loose powder remains inside the part and cannot be depowered[2]. In this way, we selectively design parts that contain zones of trapped loose powder without any binder. We will refer to zones of loose powder without any binder as no binder zones (NBZ) and zones with binder as binder zones (BZ). To achieve these NBZ, the CAD file imported to the printer is modified such that loose powder is trapped within BZ regions: NBZ regions are obtained by prescribing a cavity with no material in the CAD model, and BZs are obtained by prescribing material to be printed. To visually illustrate the method described and compare it with a standard printed sample, a CAD model of BZ *(traditionally printed part)* and NBZ surrounded by BZ regions is shown in Figure 6(a.ii) and (a.iii), respectively. These samples are later used as a benchmark to observe the effect of channel size, orientation, sintering direction, etc., therefore, we name the parts as BZ control and NBZ control. The printed samples were cross-sectioned in the XZ plane (Figure 6(a.ii, a.iii)) using wire EDM machining for phase fraction analysis.

Microstructural analysis of NBZ and BZ regions reveals that SS420 distribution in BZ remains consistent throughout (Figure 6(b)), i.e. 60% SS420 and 40% bronze adhering to the composition ratio provided by the printer supplierClick or tap here to enter text.. Conversely, the phase fraction of the NBZ control depends on the distance from the bottom of the sample in the printing direction (Figure 6(c)). At the bottom of the NBZ, the phase fraction of SS420 is 25% higher than the BZ, and at the top of the NBZ, SS420 is 6.5% higher than the BZ.

During the printing process, after each layer of powder is deposited, a roller horizontally sweeps through the build platform to level the powder. The roller exerts a vertical force on the layer of powder, which compacts the loose powder in the NBZs. The lower layers in the sample have been compacted more times by the roller than the higher layers, since the lower layers are compacted for every layer above them, and loose powder particles can travel downward due to gravity. We hypothesize that this is why there is a gradient in phase fraction with height from the bottom face in the NBZ. Given that the BZs are held together with a binder during layer deposition, this effect does not happen in the BZs resulting in a constant phase fraction of constituent materials in the final part.

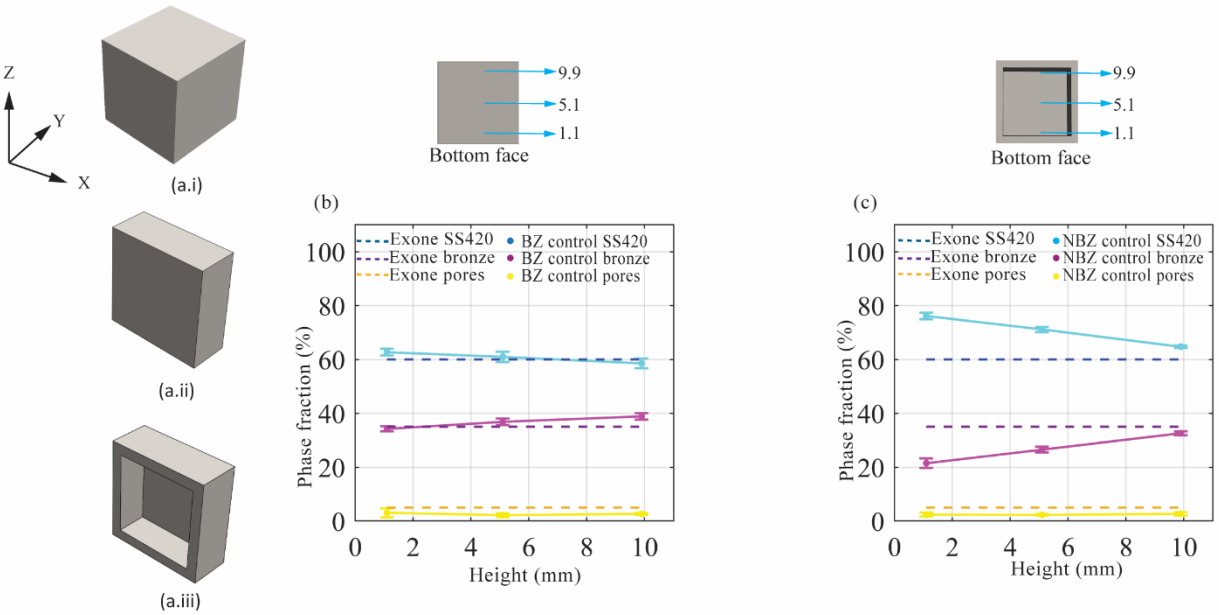

Figure 6. Modifying CAD model for binder jet printing to precisely control the spatial distribution of phases. (a.i) CAD model of the full cubic part, (a.ii) cross sectional view of BZ in the XZ plane, (a.iii) cross sectional view of NBZ in the XZ plane. Resulting phase distribution for (b) BZ control, and (C) NBZ control with variation of height towards printing direction (samples were printed to the Z direction)

The effect of NBZ channel orientation is observed with 1 mm vertical (1 mm VC) and horizontal channels (1 mm HC), respectively. These parts are designed such that each BZ channel is immediately followed by an NBZ channel, and vice versa (Figure 7 subplot). This alternating pattern facilitates a comparative analysis of how the orientation of these channels influences the overall control of phase distribution.

Optical microscopy image analysis reveals that the phase distribution of BZ channels in both HC and VC channels is identical to that of the BZ control. Further, the phase fraction of BZ channels is statistically the same as that of the BZ control, i.e., SS420 concentration is 62%, and the phase fraction does not depend on height (Figure 7(a,c)). This means that the addition of NBZ channels does not affect the BZ phase fraction. The phase distribution of the NBZ channels in VC sample (NBZ on Figure 7(b)) resembles that of the NBZ control (Figure 6(c)). The average SS420 concentration is 72% in NBZ channels, and the dependence of phase fraction on height is similar to that in the NBZ control sample.

However, the 1mm HC NBZ exhibits different patterns in phase distribution compared to the NBZ control. The phase distribution of SS420 in 1 mm HC NBZ is constant at various heights (Figure 7(d)) which is 72% SS420 - similar to the average SS420 phase in NBZ control and VC NBZ channels, however, does not depend on the channel height.

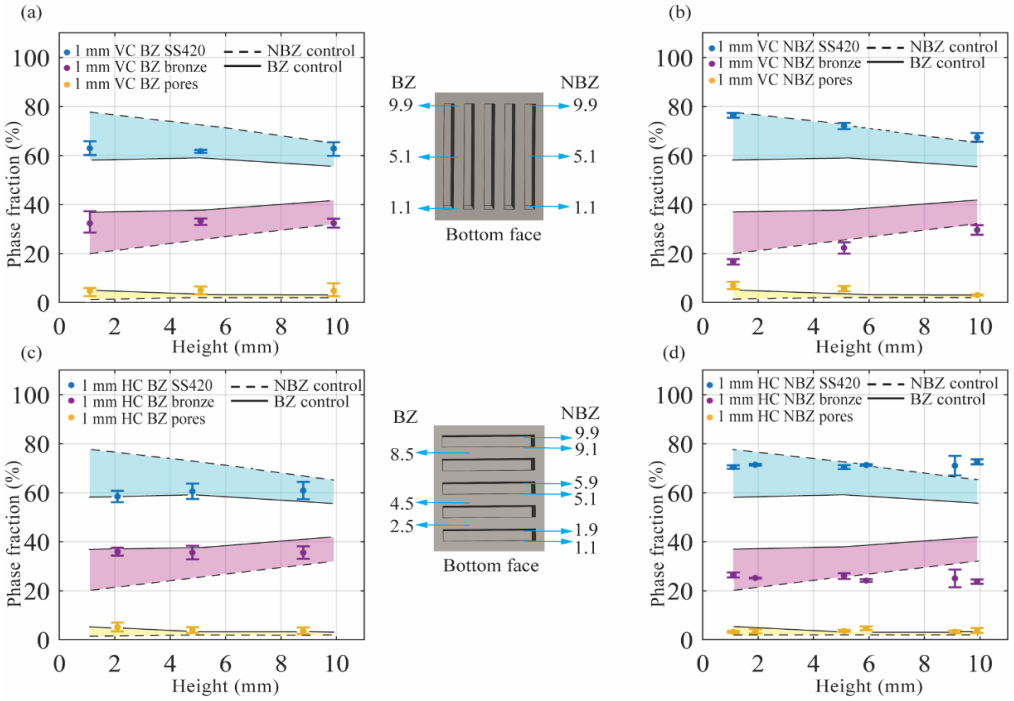

Figure 7. Spatial phase fraction variation in 1 mm VC and HC samples. Phase variation in 1 mm VC sample (a) BZ, (b) NBZ channels. Phase variation in 1 mm HC sample (a) BZ, (b) NBZ channels.

In the 1 mm VC, powder particles in the NBZ have more space to travel towards the bottom due to gravity compared to particles in the NBZ in the 1 mm HC and powder particles in the bottom of 1 mm VC are more compacted as they have more layers on top. Thus, there is a gradient in phase fraction in 1 mm VC NBZ, i.e., the phase fraction depends on height, whereas the phase fraction in 1 mm HC NBZ remains constant with height. We can approximate this variation of phase fraction related to the sample distance from the bottom face with the following equation:

$$V = y_1 + (y_2 - y_1)d \qquad (1)$$

where, V = phase fraction, y_1 = phase fraction of constitutive component at the bottom, y_2 = phase fraction of constitutive component at the top, d = height factor (bottom denoting 0 and continuously increasing to 1 at the top of a channel).

Our study also reveals that the sintering direction relative to the printing direction impacts the phase fraction. Sintering in the opposite direction of printing can counteract the height-dependent gradient observed in vertically oriented channels, resulting in a uniform phase fraction across the sample. Furthermore, by varying the channel size of NBZ we demonstrate that the phase fraction can be controlled down to a certain dimension, below which the binder spreads into the NBZ channels. Powder spreading and packing during the printing process in the BZ and NBZ is the fundamental factor of the phase fraction variation in this method.

To provide an example of the mechanical properties that could be achieved with this fabrication approach, we measured Rockwell B hardness (using a Wilson Rockwell Hardness Tester) of all the fabricated samples following ASTM E18-1541 at different heights within the specimens. Here, we highlight the differences in hardness between Binder Zone (BZ) and No Binder Zone (NBZ) controls, showcasing representative results from these assessments. The measured hardness is higher in the stainless steel-rich regions than those with less stainless steel, which qualitatively correlates with the phase fraction values measured by optical microscopy. The BZ control has a spatially uniform phase fraction, and our measurements show that their hardness is also spatially uniform (Figure 8). The hardness

of the NBZ control sample varies with height (~9% variation within NBZ) (Figure 8(b)) which is consistent with phase fraction varying with height (Figure 6(c)).

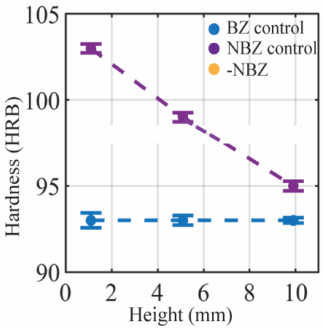

Figure 8 Variation of Rockwell B hardness (using a Wilson Rockwell Hardness Tester) with spatial phase distribution in BZ and NBZ control.

Control of fracture using binder jet MMCs:

In areas where the concentration of SS420 is higher, particles are observed to be more closely packed, resulting in enhanced interconnectivity between them. On the other hand, regions with a reduced presence of SS420 exhibit decreased interconnectivity. Furthermore, bronze is recognized for its higher ductility compared to SS420, making it more susceptible to crack propagation[1]. Our hypothesis is that the densely packed steel particle arrangement combined with the distribution of the ductile bronze phase will influence the crack propagation behavior and modulate the fracture properties of binder jet-printed MMCs. The gradient in the phase fraction of SS420 and bronze in NBZ channels introduces a gradient in mechanical properties across the height of the part. Thus, controlling such gradients within a structure can potentially influence the stress distribution within the material under load, affecting crack initiation and propagation. I have already conducted preliminary fracture measurements on these samples, and observed the crack propagation through NBZ control with SS420 gradient, shown in Figure 9. Increased crack deviation was observed in SS420 rich region, and the deviation decreased with the decreasing % of SS420. However, further experimental data is needed to conclusively demonstrate these findings.

Furthermore, a crack initiated in a region with higher fracture toughness may be arrested, deflected, or form microcracks upon reaching a region with different properties. We aim to tailor the microstructure to understand pathways of less/higher resistance for crack propagation, effectively tailoring the fracture behavior of binder jet-printed MMCs.

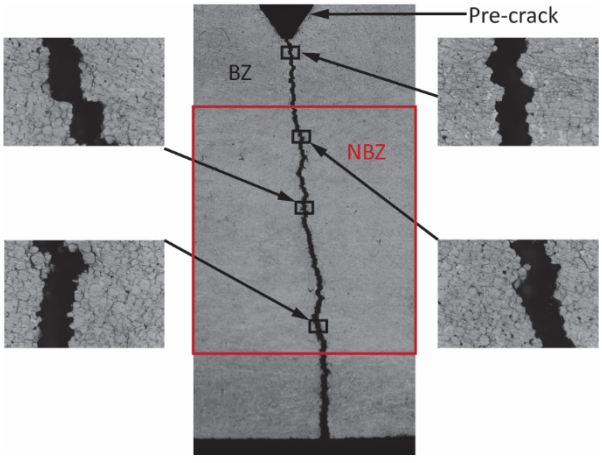

Figure 9: Crack propagation through NBZ control sample.

2. Task 2: Experimental characterization of smart composites from micro- to macro-scales

2.1 Dynamic Magneto-mechanical analysis (DMMA) of MAEs

Magneto-active elastomers (MAEs) are soft composite materials comprising ferromagnetic particles in an elastomer matrix which exhibit a magnetically-induced effective modulus change. The change in effective modulus has been experimentally studied in many MAE formulations using several different techniques; however, this makes comparisons between studies difficult, and there lacks a com- prehensive study on the dynamic magneto-mechanical properties of MAEs. In this work, we systematically investigate the effect of mechanical loading direction and magnetic field orientation on the dynamic magneto-mechanical response of isotropic and anisotropic MAEs, using a single elastomer-particle combination and specimen geometry to control for any variation due to elastomer/particle properties or structural effects. We develop a new apparatus to perform dynamic mechanical analysis of MAEs at frequencies up to several hundred hertz and in the presence of magnetic fields of varying strength, and study the effects of particle volume fraction, isotropy, and magnetic field orientation on the complex Young's modulus. Our results show the particles increase the isotropic complex modulus by up to three times and the anisotropic complex modulus by up to 65 times compared to pure elastomer. Of all configurations studied, the longitudinal Young's modulus of anisotropic MAEs exhibits the largest absolute magnetically-induced change while the transverse Young's modulus exhibits the largest relative change. The magnetically-induced change in loss factor depends on anisotropy and loading condition: isotropic MAEs have no change in loss factor while anisotropic MAEs become less lossy at low strain amplitudes but more lossy at high strain amplitudes. These results provide new insights into the fundamental mechanisms by which microstructure and magnetic field interact to affect the effective properties of MAEs.

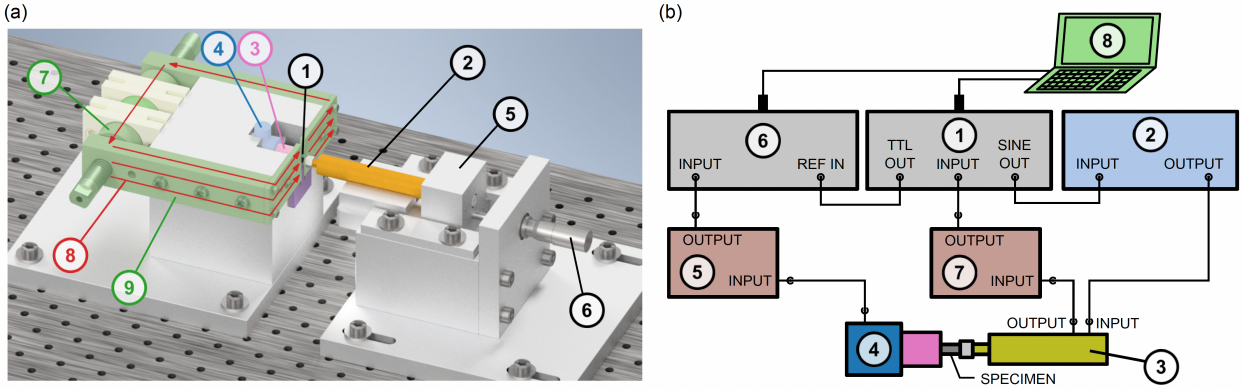

Figure 10: Custom apparatus for dynamic magneto-mechanical analysis of MAEs: (a) mechanical design of setup, and (b) schematic of instrumentation and electrical connections.

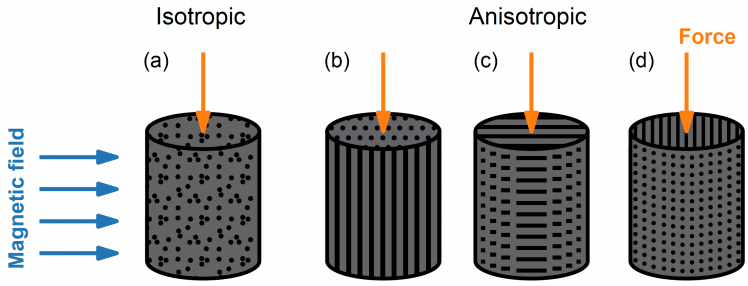

Fig 11: Sample orientations that can be tested with the DMMA setup: (a) isotropic MAEs, (b-d) anisotropic MAEs in (b) "longitudinal", (c) "transverse (∥)", and (d) "transverse (⊥)" orientations. Particle chains are indicated with black lines, applied magnetic field and applied force are indicated with blue and orange arrows, respectively.

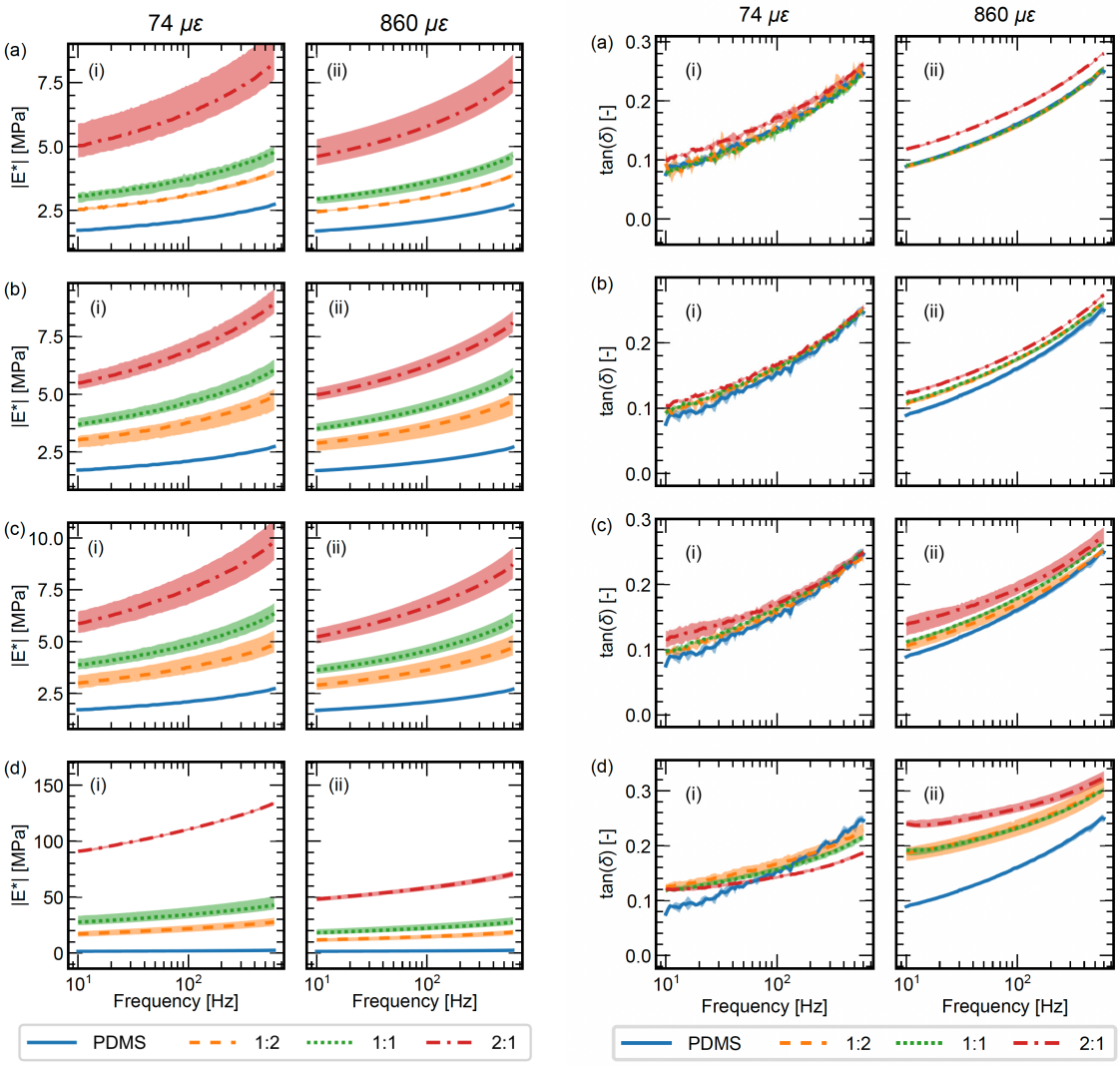

Figure 12: Storage modulus (left) and loss modulus (right) of MAEs at 0T magnetic field as a function of frequency and at two distinct strain amplitudes. Frequency dependence is shown for all orientations: (a) isotropic, (b) transverse (∥), (c) transverse (⊥), (d) axial. Each column represents tests conducted at a different strain amplitude as indicated at the top of each column.

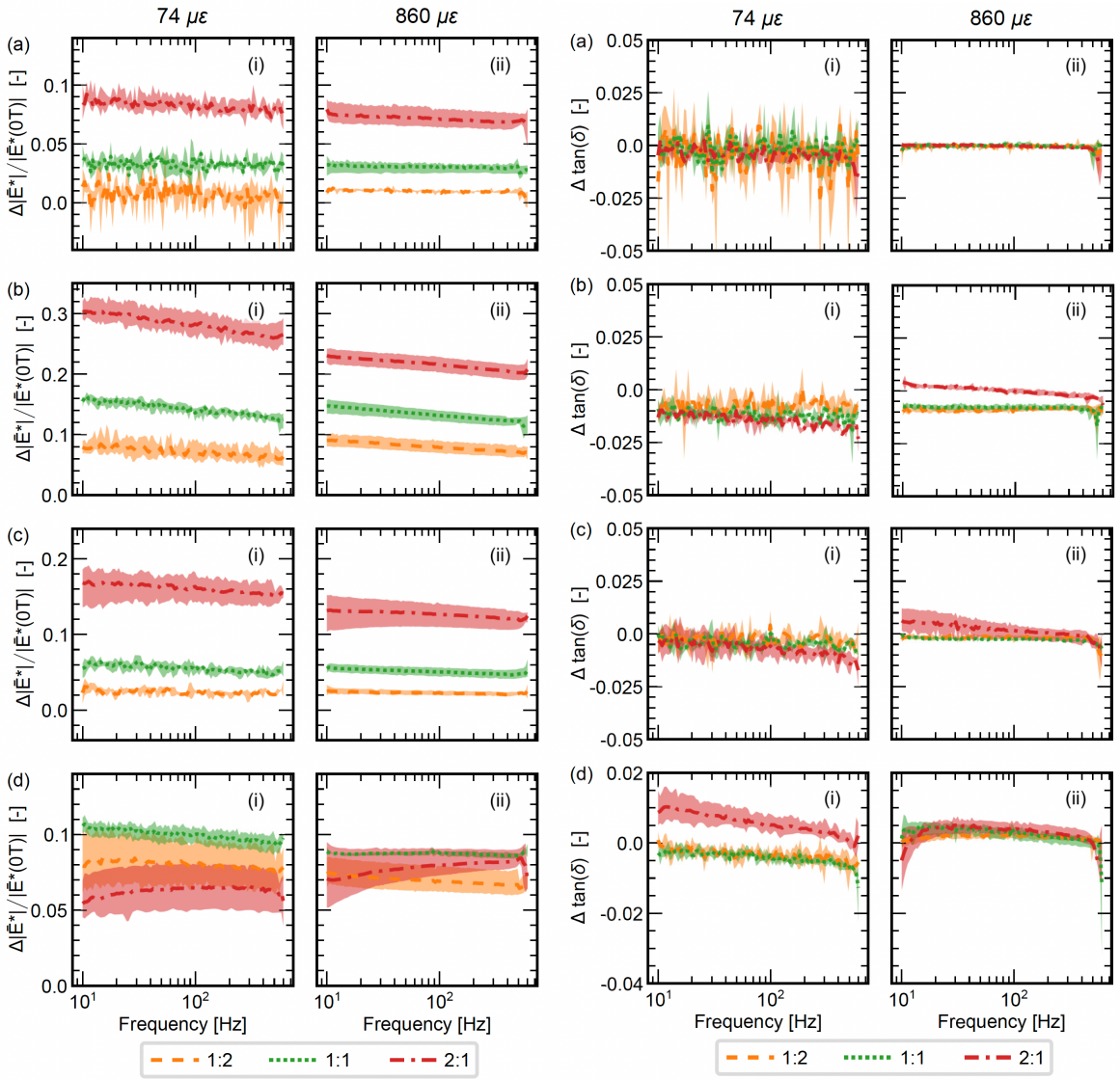

Fig 13: *Normalized change in MAE storage modulus magnitude (left) and loss modulus (right) induced by a magnetic field of 0.17T. Frequency dependence is shown for all orientations: (a) isotropic, (b) transverse (∥), (c) transverse (⊥), (d) axial. Each column represents tests conducted at a different strain amplitude as indicated at the top of each column.*

2.2 Fracture toughening mechanism and crack propagation in MAEs: effect of iso/anisotropy on onset of crack propagation and fracture toughness

We characterized the effect of anisotropy and chain orientation on the fracture properties of MAEs. It was observed that the degree and direction of anisotropy profoundly influence the fracture toughness of MAEs. Anisotropic MAEs with particle chains oriented at 0° to the applied load exhibited the highest enhancement in fracture toughness, while the 90° orientation showed the least enhancement. Intermediate orientations, such as 45°, displayed fracture toughness values falling between those of 0° and 90° orientations. The observed trends were consistent across all volume fractions, whereas isotropic sMAEs did not exhibit any trend relating to % vol. CIP, indicating a robust relationship between fracture toughness and the directional orientation of particle chains demonstrated in Figure 2(a). The variation in fracture toughness is attributed to the interplay between material stiffness and stretch to failure

determined by the onset of crack propagation, which varies significantly depending on the orientation of the particle chains relative to the applied load (shown in Figure 5).

Also, the fracture toughness of sMAEs increases monotonically with the % vol. CIP for both isotropic and anisotropic cases. In the anisotropic configurations, especially at 0° where particle chains are aligned parallel to the load direction, there is not only an increase in material stiffness but also a notable increase in stretch to failure with % vol. CIP, leading to a marked increase in G_c. This contrasts with other configurations, where the stretch to failure shows no clear dependence on % vol. CIP, and the enhancement in fracture toughness is primarily governed by changes in stiffness alone. The load response curves of anisotropic 0° and 90° as a function of % vol. CIP are demonstrated in Figure 14 (corresponding effect on fracture toughness shown in the subplots). These two plots are representative examples, showing the response characteristics exhibited by the broader range of configurations evaluated in this study.

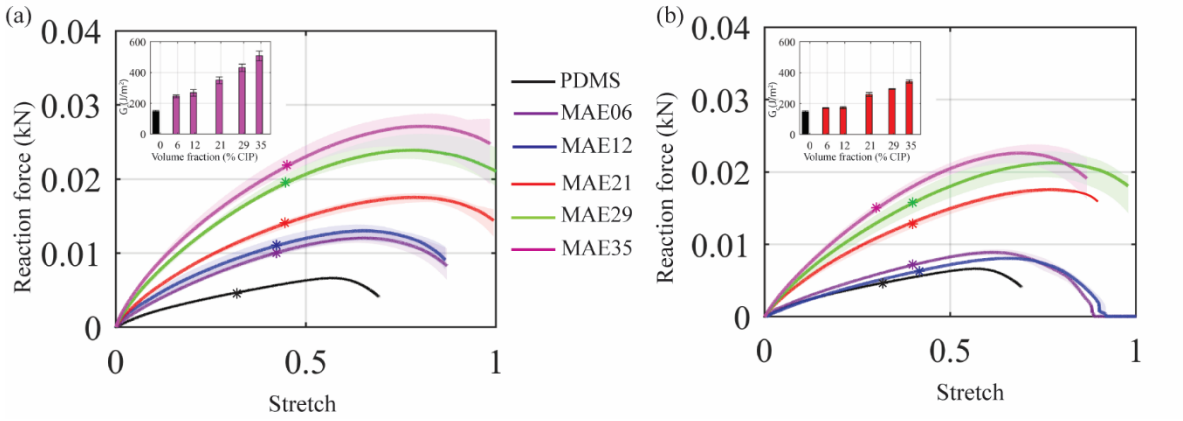

Figure 14 Load response curves of (a) anisotropic 0°, and (b) anisotropic 90°. Asterisks demonstrating the onset of crack propagation. Subplots exhibit fracture toughness behavior corresponding to the load-response curves.

SEM image analysis correlates fracture toughness and onset of crack propagation with fractured surface morphology:

SEM image analysis of the post-fractured surface near the initial crack tip provides insights into crack propagation behaviors influenced by CIP distribution and orientation. An elaborate analysis of SEM images across all configurations elucidates that both fracture toughness and load response can be discerned from these images. A representative analysis for sMAE06 is provided in this section.

Isotropic configurations of sMAEs show a direct relationship between the heterogeneity of CIP distribution and the mechanisms of crack deviation, pinning, and particle pullout (Figure 15(a)). These mechanisms are indicative of the energy-absorptive fracture process. The presence of particle agglomerations within these isotropic samples suggests that certain distributions can facilitate easier crack propagation, potentially affecting the irregular onset of crack propagation mentioned in section 2.1.2. This highlights the dual role of CIP distribution: enhancing toughness through energy-consuming mechanisms while possibly undermining it through less effective particle-matrix interactions due to presence of agglomeration.

In anisotropic sMAEs, particularly those with CIPs oriented at 0°, the organized distribution of particle chains perpendicular to the crack propagation plane leads to a significantly increased incidence of crack deviation and pinning (Figure 15(b)). This ordered arrangement enforces a more tortuous crack path, substantially elevating the fracture toughness. The uniformity of particle distribution in this configuration minimizes the occurrence of detrimental agglomerations within the crack plane, ensuring a consistent enhancement in material toughness and a consistent trend of onset of crack propagation with % vol. CIP.

Conversely, in the 90° anisotropic configuration, SEM imaging illustrates that cracks tend to align with the particle chains, navigating through the matrix in a manner that reflects the directional distribution of CIPs (Figure 15(c)). Moreover, waviness in chains thus in crack path is observed that forms a larger radius of curvature at lower % vol. CIP (i.e., sMAE06, sMAE12) and smaller radius of curvature at a higher % vol. CIP (i.e., sMAE29, sMAE35). Further, the agglomeration lies in the particle chain direction in 90° MAEs, thus, in the direction of crack propagation. This strongly influences the irregular onset of crack propagation in this MAE configuration.

For the 45° anisotropic sMAEs, the crack propagation behavior aligns with that of the 90° orientation despite the angular particle chain distribution (Figure 15(d)). This suggests that the waviness present in particle chains at this configuration tends to align some of the chains in the crack propagation direction. A detail analysis reveals that anisotropy, waviness in particle chain, and particle agglomeration play pivotal roles in modulating fracture properties. By leveraging the directionality of particle chains, it is possible to significantly influence the crack response of sMAEs, underscoring the critical importance of anisotropy in optimizing fracture toughness and mechanical behavior.

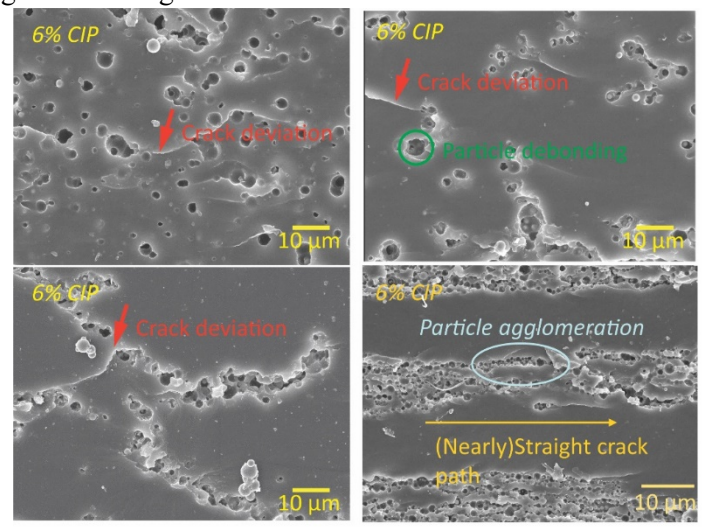

Figure 15 SEM images revealing crack deviation, particle debonding on post-fractured surface regulated by CIP distribution. (a) Isotropic, (b) anisotropic 0°, (c) anisotropic 45°, and (d) anisotropic 90° sMAE12.

3. Task 3: Experimental characterization of crack propagation in smart composites:

3.1 Dependence of fracture properties of MAEs on external magnetic field

To further explore the fracture mechanics of sMAEs, fracture tests were performed while applying an external magnetic field. This experimental setup aims to understand how an external magnetic stimulus affects the fracture properties of sMAEs, thereby assessing the influence of magnetically induced anisotropy on crack propagation and overall material toughness. A setup was made with 0.3 T generated by two permanent magnets and was incorporated with the tensile testing setup shown in Figure 16(a). A similar method as mentioned in section 2.1.1 was used to measure the fracture toughness and observe the initiation of crack propagation. The fracture toughness results of magnetized samples compared with the unmagnetized counterparts are shown in Figure 16(b) which demonstrates that anisotropic 0° at high % vol. CIP shows a significant impact of magnetic field on fracture toughness, while the change in fracture toughness in other configurations is not as pronounced.

The post-fractured surface was analyzed with SEM and showed qualitatively identical crack propagation behavior with sMAEs that were not magnetized during the test. The analysis holds for every configuration at each volume fraction confirming that any change in fracture properties does not stem from modifications in the crack propagation paths but rather from the internal mechanisms stemming from the response of sMAEs to the magnetic field. A representative comparison of SEM images between magnetized and unmagnetized samples is shown in Figure 16(c), however, a significant change in the load response curve is observed for magnetized sMAE35 anisotropic 0° compared to the unmagnetized counterpart. The onset of crack propagation did not change significantly, while it is observed that stiffness has changed significantly.

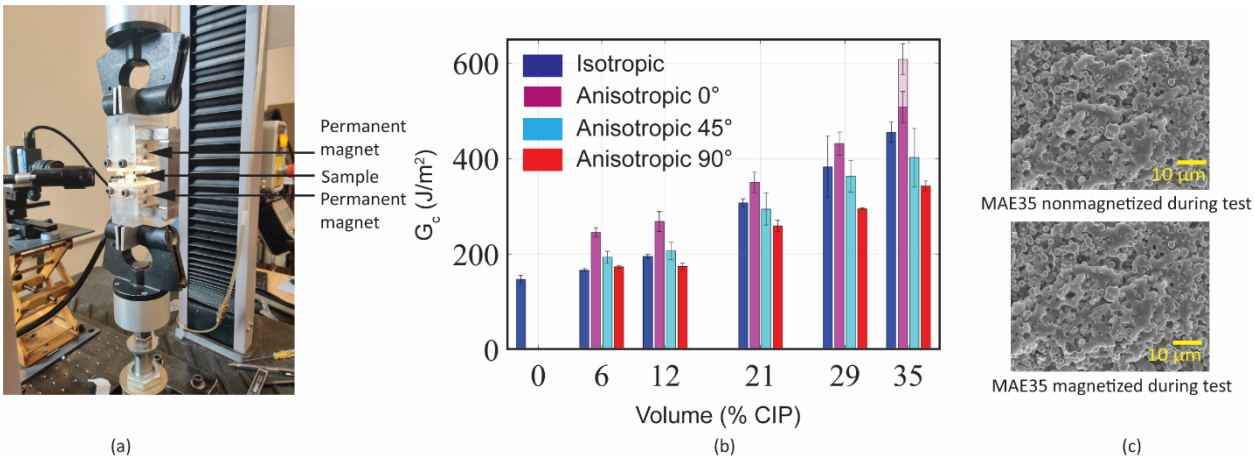

Figure 16: Analysis of sMAE fracture under external magnetic field. (a) Experimental test set up, (b) fracture toughness results compared with unmagnetized sMAEs, and (c) SEM images of sMAE35 anisotropic 0°.

DIC images provided a clearer understanding of how the toughening mechanisms in sMAEs are influenced by the orientation of anisotropic particle chains within the material. In the anisotropic 0° configuration, the alignment of the magnetic field and the mechanical load with the particle chain direction leads to a notable enhancement in fracture toughness (Figure 16(b)). This enhancement is attributed to the effect of the magnetic field on the crack tip, which tends to close or reduce the crack opening under magnetic influence (Figure 17(a)), this effect is termed as crack tip shielding. The magnetic field exerts forces on the magnetically responsive particles aligned in chains, pulling the particles toward each other. This action can effectively reduce the crack opening or even partially close

the crack at the tip, increasing the resistance to crack propagation. As a result, the energy required to propagate the crack increases, thereby increasing the fracture toughness.

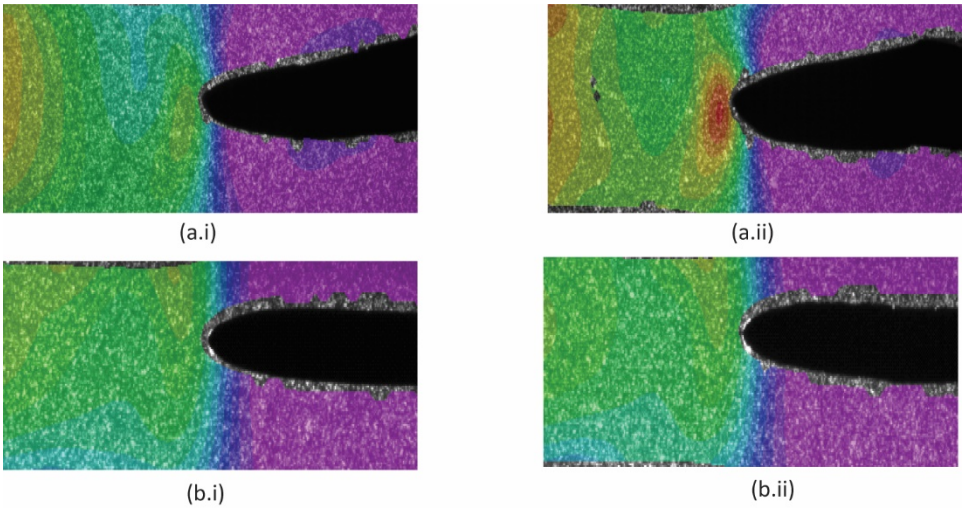

Figure 17 DIC images illustrating strain response of pre-cracked sample to external magnetic field compared to unmagnetized MAE. (a.i) unmagnetized MAE35 anisotropic 0°, (a.ii) magnetized MAE35 anisotropic 0°, (b.i) unmagnetized MAE35 isotropic, and (b.ii) magnetized MAE35 isotropic.

For configurations other than anisotropic 0°, such as anisotropic 90° (where the magnetic field and mechanical load are perpendicular to the particle chain direction) or isotropic distributions, the crack tip shielding effect induced by the external magnetic field is not as pronounced. In these cases, the magnetic forces acting on the particles do not contribute as effectively to closing the crack tip. The particle distribution/chains in these configurations do not align in a way that the magnetic field can significantly influence the crack opening. Therefore, the unique crack tip closure effect observed in the anisotropic 0° configuration is largely absent. A representative illustration is shown in Figure 17(b). The limitation of this experiment is investigating the crack tip shielding effect at higher magnetic fields, due to the constraints in generating sufficiently strong magnetic fields.

3.2 Brick-and-Mortar Structures

Due to the difficulties encountered in direct-ink write of vitrimer epoxy, we next studied an aluminum-MAE material system to fabricate magnetoactive architected structures for fracture control, with aluminum "bricks" and MAE "mortar". To ensure a strong bond between the bricks and mortar, we formulated the MAE from an elastomer adhesive. We performed tensile tests which showed that the aluminum-MAE bond was stronger than the failure strength of the MAE, indicating that failure of an aluminum-MAE architected geometry should be dominated by cohesive failure of the MAE rather than adhesive failure of the aluminum-MAE bond. This suggests that aluminum-MAE is a promising material system to fabricate architected geometries for crack control.

We fabricated an aluminum-MAE brick-and-mortar geometry as shown in Figure 18(a) via an injection-molding technique and performed double edge-notched fracture tests on the fabricated structure. In contrast to our MAE-aluminum tensile bond tests, failure in the brick-and-mortar structure was via debonding between the bricks and mortar as shown in Figure 18(b-c), and not via crack propagation from the edge notches in the mortar. We subsequently investigated numerous surface preparation techniques for the aluminum bricks, and further fracture tests of these structures are ongoing.

Figure 18: (a) architected brick-and-mortar structure fabricated from aluminum “bricks” and MAE “mortar”. (b) In a double edge-notched fracture test, debonding initiated at brick-mortar interfaces and (c) failure occurred when the debonding spread to neighboring bricks.

4. Task 4: Finite Element Modeling of smart MAE composites

4.1 Crack deviation in MAEs using far-field stresses induced by magnetostriction

We developed a phase-field model of fracture that includes magneto-mechanical coupling in MAEs. Using these models and the measured MAE properties, we studied magneto-mechanical interactions under different arrangements of magnets. We aim to show that we can control crack propagation through far-field stresses induced by magnetostriction. One configuration was of particular interest and yielded some promising results. By placing a set of magnets in an antisymmetric disposition with respect to crack planes, we can use magnetic fields to induce a Mode II stress field at the crack tip (Fig. 19a). When the specimen is pulled with a Mode I mechanical load, mixed-mode fracture occurs at the crack tip resulting in a change in crack propagation direction (Fig. 19b). By controlling the separation between the magnets, we can change the magnetic field intensity and thus control the crack propagation direction (Fig. 19c). This setup can be used either to avoid a crack to reach a critical component or to test MAEs under mix mode fracture conditions.

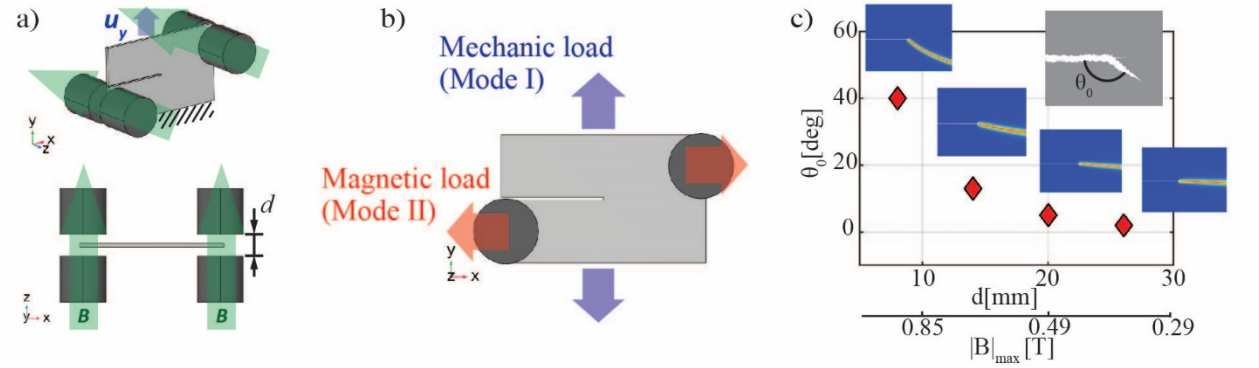

Fig. 19. a) Magnet configuration (green arrows show the direction of the magnetic field). b) Schematic of mechanical and magnetic loads. c) Dependance of crack propagation direction on magnetic field calculated using a phase-field model. Insets show phase-field model results. The red color in insets represents the damaged regions.

Although numerical results seem promising, experimental validation and implementation of this configuration were not yet possible since the magnetic field is perpendicular to the specimen thickness. This results in a strong attraction of the sample towards the magnets when the MAE sample is slightly off-centered, changing the boundary conditions in the experimental setup (Fig. 20). In addition, the phase-field models developed do not yet include critical surface tractions induced by the magnetic fields as well as the effects of changes in permeability in cracked regions as the crack propagates. Future work will further develop the phase-field models for a more accurate predictions and investigate the different magnetic configurations to avoid out-of-plane displacements and ease the experimental validation and application of the proposed method for damage control.

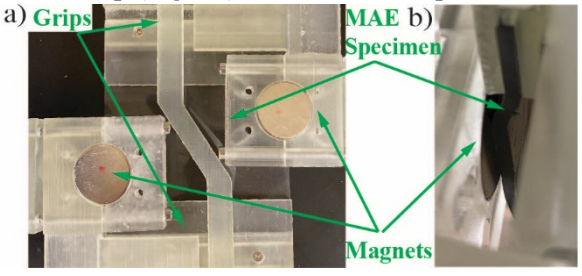

Fig. 20. Setup for validation of crack deviation. b) Front view. b) Close-up of side view shows large out of plane displacements of the MAE.

4.2 Analysis of crack propagation through 2D benchmark simulation

The 2D benchmark simulations, employing the Phase Field-Cohesive Zone Model (PF-CZM), offer insights into crack propagation behaviors across sMAEs with varied CIP distributions and volume fractions. These simulations, focusing on isotropic configurations and anisotropic alignments at 0° and 90° relative to the loading direction, aim to establish a baseline understanding of how crack trajectories

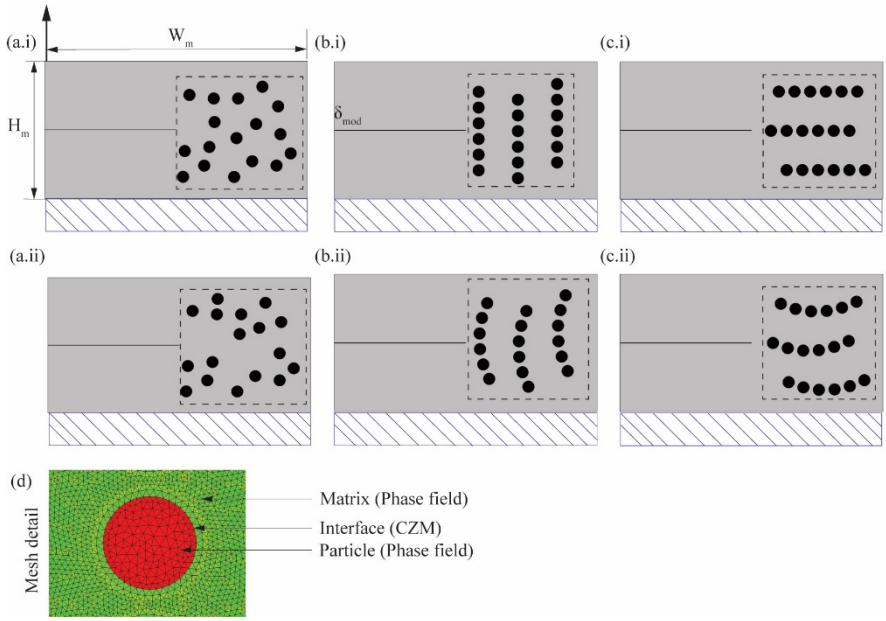

Figure 21: Details of computational model used to study the crack propagation behavior in composites. (a) isotropic MAE - (a.i) particles closely spaced in the crack path and (a.ii) particles remotely spaced from crack path, (b) anisotropic 90◦ - (b.i) straight chain and (b.ii) wavy chain, (c) anisotropic 0◦ - (c.i) straight chain and (c.ii) wavy chain. The zones shown in box in (a-c) are modeled as heterogenous and the rest are modeled as PDMS. Hashed lines denote fixed support. (d) Close-up view of the finite element mesh

are influenced by microstructural anisotropy (selected configurations at higher % vol. CIP are shown in Figure 21). By leveraging SEM-measured properties to model both straight and wavy anisotropic particle chains, the study provides a comparative analysis of crack propagation mechanisms inherent to different MAE configurations bridging a relation with individual fracture toughness.

For isotropic sMAEs, simulations reveal that the proximity of CIPs to the crack path significantly impacts crack deflection, with closer particles inducing greater deviation. This observation aligns with SEM analyses, which show increased crack deflection at higher CIP volume fractions. In contrast, when particles are farther from the crack path, there is a noticeable reduction in crack deflection, underscoring the critical role of particle distribution in influencing fracture behavior. We measure the crack path length from simulation and plot them with experimentally measured fracture toughness to demonstrate the relationship between crack path length and energy absorption (Figure 22).

Anisotropic sMAEs at 0° exhibit pronounced crack deviation due to straight and wavy chain configurations, with wavy chains at higher volume fractions causing the most significant deviation from a straight crack path. This deviation is attributed to the intricate interplay between crack-particle interactions and the geometrical constraints imposed by particle alignments. Thus, we observe the higher fracture toughness for sMAE35 anisotropic 0° attributed to a longer crack path (Figure22).

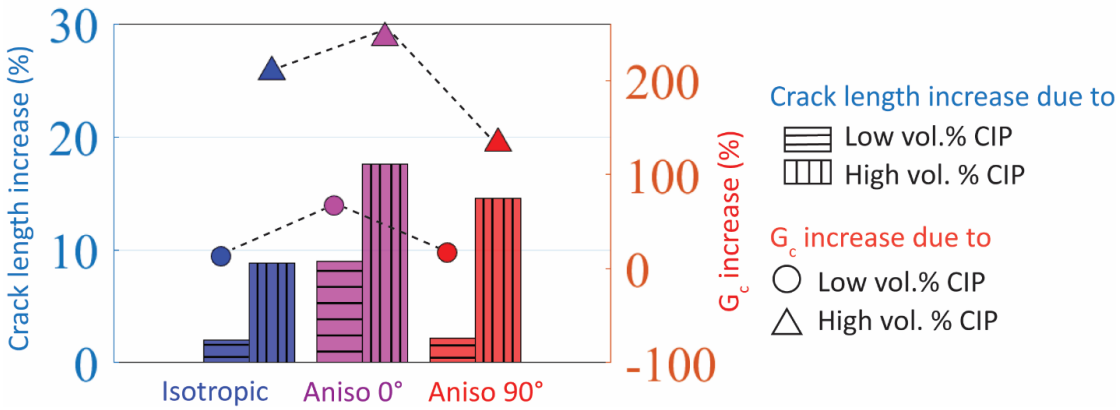

Figure 22: Crack path length and fracture toughness of various sMAE configurations at low and high % vol. CIP.

Notably, the simulation results for anisotropic 90° sMAEs demonstrate that straight chains parallel to the crack propagation direction facilitate smoother crack paths, making this configuration possess the lowest fracture toughness at a particular volume fraction compared to other anisotropic sMAEs. However, wavy configurations introduce greater deviation, especially at higher volume fractions. Thus, we expect a higher fracture toughness at this % vol. CIP compared to isotropic sMAEs because the crack path length is longer, however, this is not the case in experimental fracture toughness analysis (Figure 22). The limitation stems from the omission of particle agglomeration effects in the simulation.

4.3 MAE Homogenization Modeling

Magneto-active elastomers (MAEs) are composite materials comprising an elastomer matrix with embedded magnetic particles, endowing the composite with coupled effective magneto-mechanical responses. MAEs can be prepared in isotropic formulations with random particle distributions or in anisotropic formulations with chain-like structures of particles, and it is widely reported that anisotropic MAEs exhibit much stronger magneto-mechanical coupling than isotropic MAEs. However, most efforts to model the effective magneto-mechanical properties of MAEs via homogenization approaches have focused on isotropic microstructures or microstructures which are constructed to have large separations between particles, in order to make use of analytical homogenization solutions. Such models therefore exclude by construction the microstructural effects which contribute to the enhanced magneto-mechanical coupling of chain-like anisotropic MAEs. In this work, we introduce a periodic homogenization approach to compute the effective magneto-mechanical properties of anisotropic MAEs, and use this model to analyze the microstructural features enhance their magneto-mechanical coupling. Using the finite element method, we numerically determine the effect of various microstructural parameters---including the particle shape, gap between particles, and presence of voids in the microstructure---on the effective stiffness, effective permeability, and effective magneto-mechanical coupling tensors for chain-like periodic microstructures in three dimensions. Using insights gained from the full-field simulations, we derive an analytical expression for the magneto-mechanical coupling in the chain direction, in terms of the volume fraction, gap size, and properties of the matrix and particles. Our results show that the overall magnetostriction of anisotropic MAEs is most sensitive to the gap between particles and the waviness of the particle chains, with smaller gap sizes and straighter chains yielding higher overall magnetostriction. Interestingly, our simulations show that while isotropic MAEs elongate in a uniform magnetic field, anisotropic MAEs contract with much larger strain amplitudes, a result of the attractive forces between particles being much stronger in anisotropic MAEs than in isotropic MAEs because of the close particle spacing found in anisotropic MAEs. Our results provide fundamental insights into the mechanisms that govern magneto-mechanical coupling in anisotropic MAEs, and additionally constitute a toolbox of material properties for design of magnetostrictive devices.

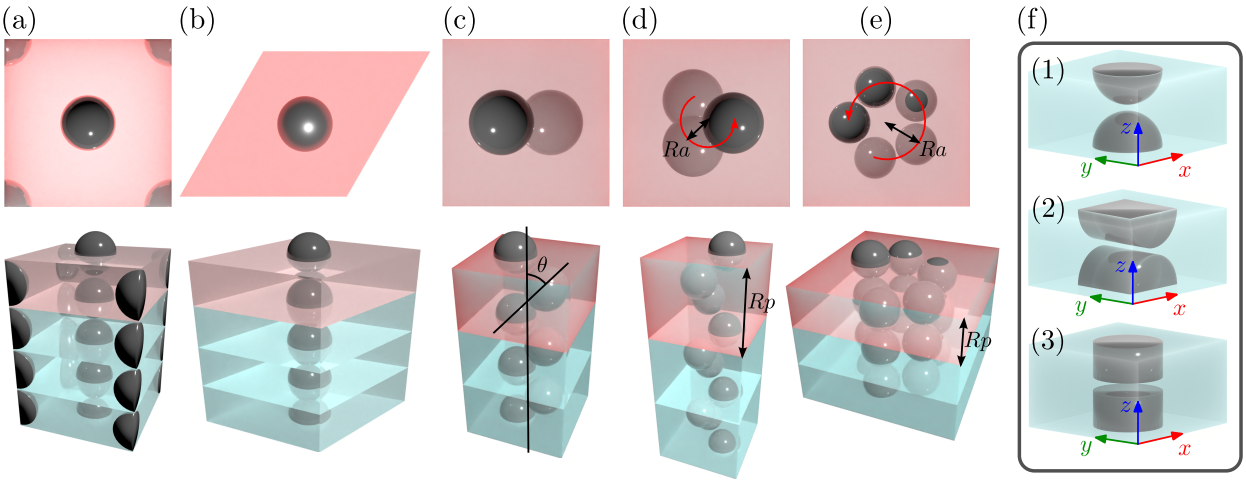

Figure 23: Unit cell geometries studied in the homogenization work.

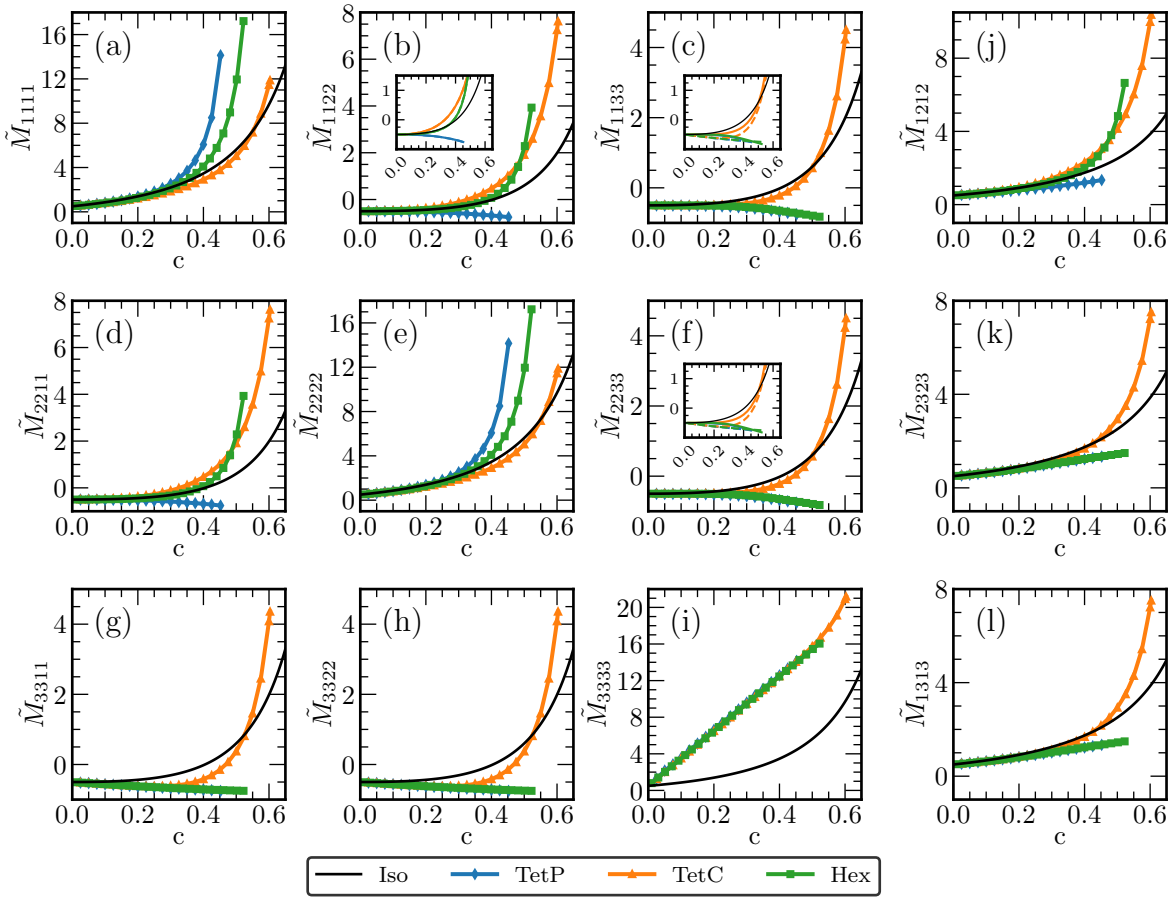

Figure 24: Nonzero components of the magnetostrictive coupling tensor for straight-chain geometries with fixed gap size d = 0.05.

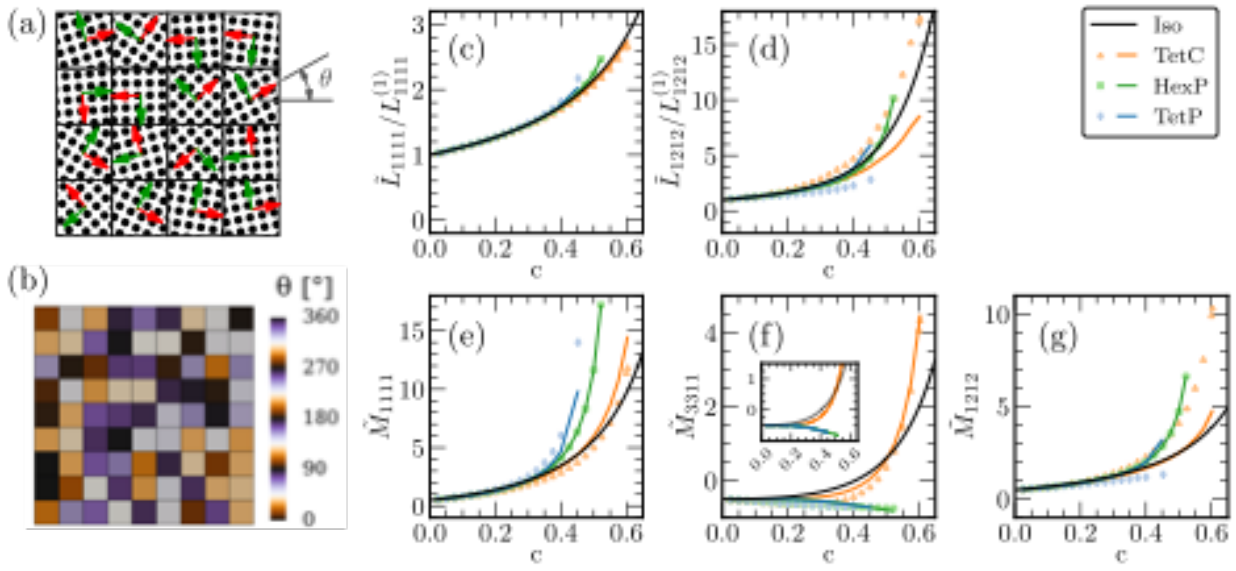

Figure 25: Transversely isotropic (TI) MAE effective properties for TetP, TetC, and Hex microstructures, computed from unit cells with grids of randomized xy-orientation. (a) schematic of 4×4 randomized unit cell and (b) implementation of a 9×9 unit cell in COMSOL Multi-physics. (c-g) effective stiffness and effective magneto-mechanical coupling. Markers indicate effective properties prior to the TI homogenization step while lines indicate TI effective properties.

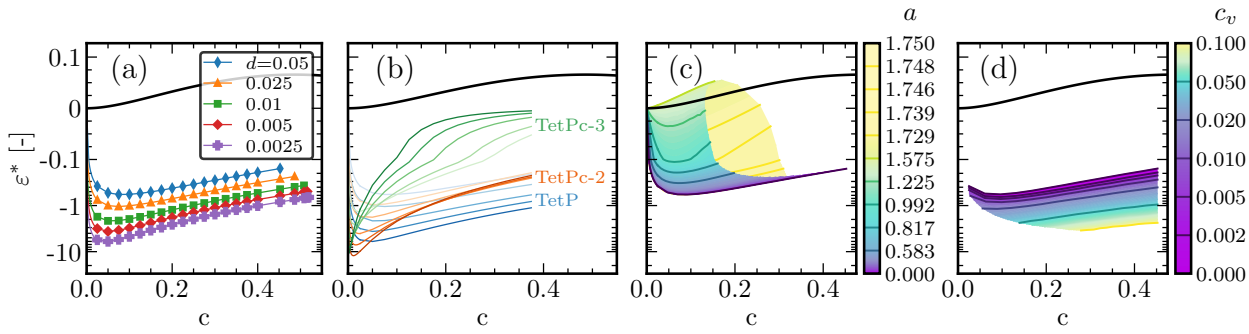

Figure 26: Magnetostriction for (a) TetP unit cell with varying gap size, (b) different particle shapes, (c) TetPs-5 spiral geometry with varying spiral radius and (d) TetPv geometry with d=0.05 and varying void volume fraction. Isotropic MAE is shown in each plot with a solid black line. Note the split log scale of the ordinate in each subplot: small strains are displayed on a linear scale, strains > 0.1 on a log scale.

5. Task 5: Characterizing band gaps in smart MAE composites

Towards our goal of linking crack propagation to band gaps in phononic materials, we developed a new method of characterizing mechanical band gaps in damped phononic materials consisting of MAEs[3]. Phononic crystals (PCs) and acoustic metamaterials (AM) have been widely reported to exhibit band gaps, which for non-dissipative systems are well-defined from the dispersion relation as a frequency range in which no propagating (i.e. non-decaying) wave modes exist. However, the notion of a band gap is less clear in dissipative systems, as all wave modes exhibit attenuation. Various measures have been proposed to quantify the "evanescence" of frequency ranges and/or wave propagation directions, but these measures lack a rigorous physical motivation. Furthermore, in finite systems created by truncating a PC or AM, wave propagation is strongly attenuated but not completely forbidden, and a quantitative measure that predicts wave transmission in a finite PC or AM from the infinite dispersion relation is elusive. In this paper, we propose a physically-motivated "evanescence indicator" that relates the decay component of the Bloch wavevector to the transmitted wave amplitude through a finite PC or AM. When plotted over a frequency range of interest, this indicator reveals frequency regions of strongly attenuated wave propagation, which are dubbed "fuzzy band gaps" due to the smooth (rather than abrupt) transition between evanescent and propagating wave characteristics. We validated the indicator using measurements of wave transmission through highly viscoelastic and finite phononic crystals.

Our general approach to defining an evanescence indicator for damped systems is as follows: first, we select a finite structure of reference for which the wave attenuation is measured, and choose a physical quantity (e.g. stress or displacement) as a measure of wave amplitude. For concreteness, we study two examples in which the displacement at a single point and the average displacement magnitude over several points are selected to characterize the wave amplitude. Next, we approximate the wave amplitude for all frequencies of interest using information directly extracted from the dispersion relation: a weighted summation of the Bloch mode shapes, so that the contributions of all wave modes are considered simultaneously. The amplitude is calculated at two locations (`input' and `output') and the normalized transmission (output divided by input) is computed. Finally, we define ``fuzzy band gaps" using a threshold value of normalized transmission as the criterion for fuzzy band gap existence: if the transmission is greater than the threshold transmission, there is no fuzzy band gap, and if the transmission is less than the threshold transmission, a fuzzy band gap is considered to exist.

The fuzzy band gap analysis was applied to simple mass spring models that include viscoelastic springs, to demonstrate the concept. Fuzzy band gap analysis was then applied to MAE metastructures, that were fabricated, tested, and analyzed in prior work in collaboration with AFRL[4]. These experimentally-determined band gaps in highly viscoelastic phononic crystals are demonstrated in the following four figures.

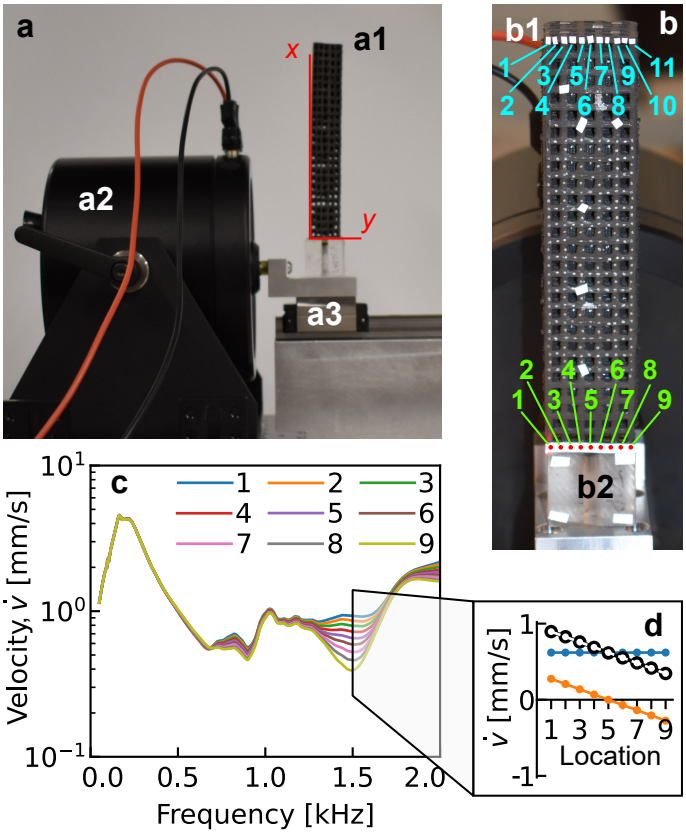

Figure 27: Experimental determination of wave transmission in an MAE metastructure for transverse excitations. (a) Side view of experimental setup. Metastructure (a1) is excited by an electrodynamic shaker (a2). A linear guide (a3) confines displacement to the y-direction. (b) Front view of metastructure indicating nine input measurement locations (b2) on the acrylic block and 11 output measurement locations (b1) on the free end of the metastructure. (c) Frequency spectrum of the input velocities. Divergence of the input velocities above 1.25kHz indicates the emergence of rigid body rotation. (d) Input mode shape at 1.5kHz: black---experimental velocity; blue---rigid body translation; orange---rigid body rotation; white markers and dashed line---superposition of rigid body translation and rotation.

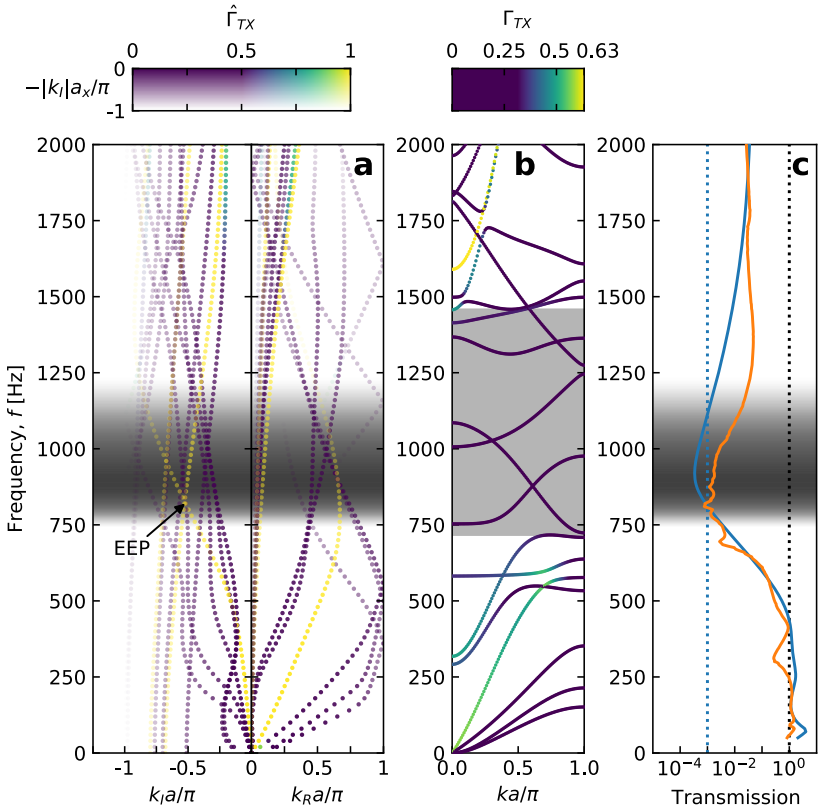

Figure 28: MAE metastructure results for longitudinally-polarized waves. (a) Damped dispersion relation, with the hue of each point determined by Γ_{TX} for the corresponding Bloch mode shape, and the transparency determined by kI, as shown in the colorbar above the plot. “Frustrated” modes have kR = 0, kI > 0 at ω = 0. The “equal evanescence point” (EEP) between the resonator and first frustrated mode is indicated by the arrow. (b) Undamped dispersion relation, with the hue of each point determined by ΓTX as shown in the colorbar above the plot. The longitudinal band gap is shaded in gray. (c) Transmission through a 5 unit cell finite structure: blue line—FEM, orange line—experimental. In (a) and (b), modes with a strong longitudinal polarization are colored yellow or green while other modes are colored blue or purple. In (a) and (c), fuzzy band gaps are computed using the evanescence indicator with N = 5 and $T_{thres} = 10^{-3}$, and the dashed blue line in (c) indicates the threshold transmission, T_{thres}.

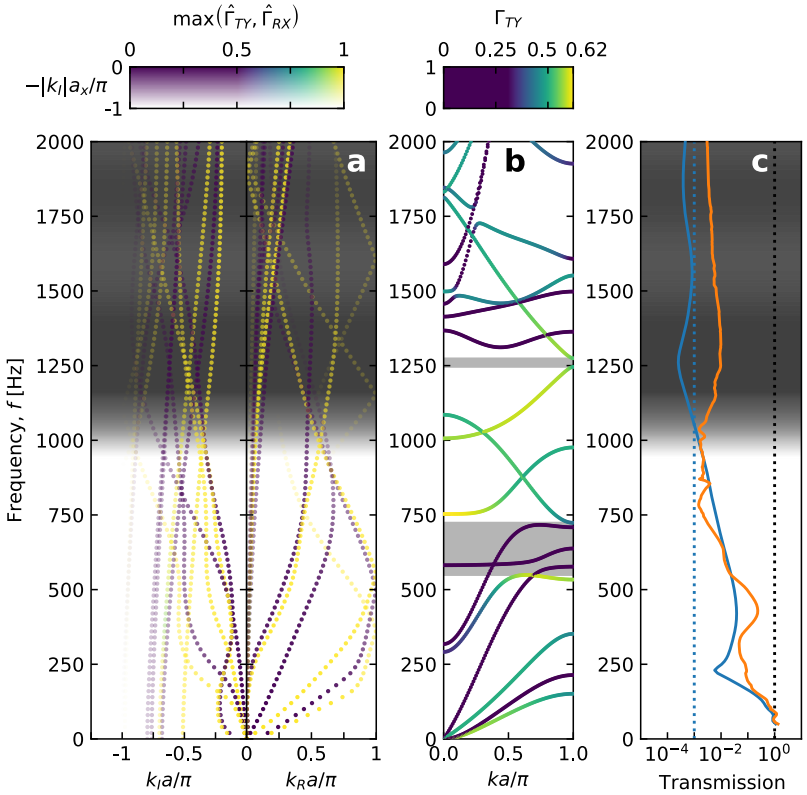

Figure 29: MAE metastructure results for transverse (y)-polarized waves. (a) Damped dispersion relation, with the hue of each point determined by the maximum value of ˆΓTY and ˆΓRX for the corresponding Bloch mode shape, and the transparency determined by kI, as shown in the colorbar above the plot. (b) Undamped dispersion relation, with the hue of each point determined by ˆΓTY as shown in the colorbar above the plot. The transverse-polarized band gaps are shaded in gray. (c) Transmission through a 5 unit cell finite structure: blue line—FEM, orange line—experimental. In (a) and (b), modes with a strong transverse polarization are colored yellow or green while other modes are colored blue or purple. In (a) and (c), fuzzy band gaps are computed using the evanescence indicator with N = 5 and T_{thres} = 10−3, and the dashed blue line in (c) indicates T_{thres}

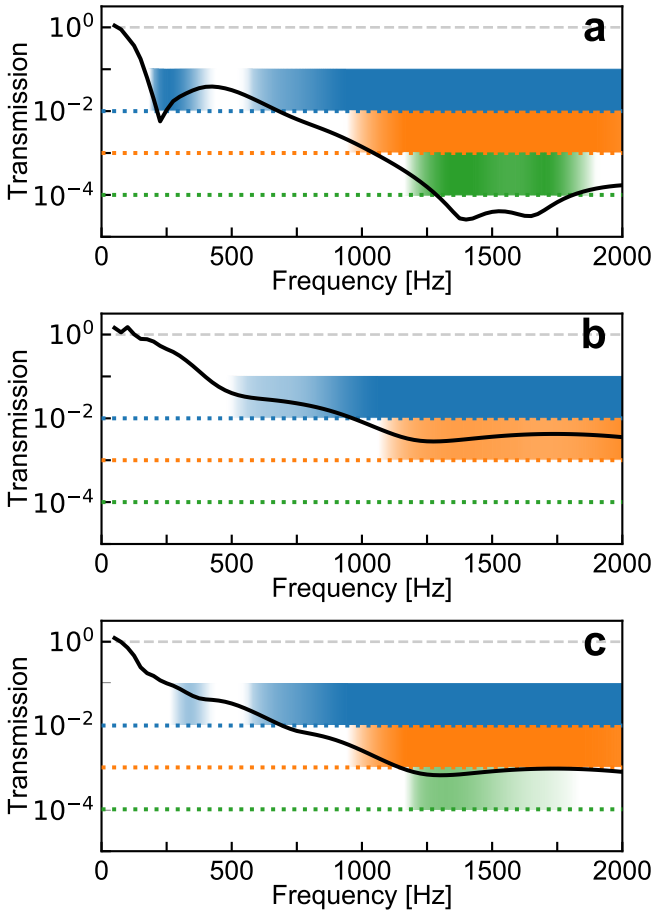

Figure 30: Polarized fuzzy band gaps in the MAE metastructure: (a) translational (y) only, (b) rotational (x-axis) only, (c) simultaneous translation (y) and rotation (x-axis). Dotted lines indicate threshold tranmission $T_{thres} = 10^{-2}$ (blue), $T_{thres} = 10^{-3}$ (orange), $T_{thres} = 10^{-4}$ (green), and solid black lines indicate FEM-simulated transmission.

References

[1] R. S. Rivlin and A. G. Thomas, "Rupture of rubber. I. Characteristic energy for tearing," *J. Polym. Sci.*, vol. 10, pp. 291–318, 1953.

[2] N. J. Salim, I. Arretche, and K. H. Matlack, "A process to spatially control the fraction of SS420 and bronze phases in binder jet infiltrated parts," *J. Manuf. Process.*, vol. 85, no. August 2022, pp. 612–622, 2023, doi: 10.1016/j.jmapro.2022.11.076.

[3] C. D. Pierce and K. H. Matlack, "'Fuzzy Band Gaps': A physically motivated indicator of bloch wave evanescence in phononic systems," *Crystals*, vol. 11, no. 1, pp. 1–26, 2021, doi: 10.3390/cryst11010066.

[4] C. Pierce *et al.*, "Adaptive elastic metastructures from magneto-active elastomers," *Smart Mater. Struct.*, vol. 29, no. 065004, pp. 1–11, 2020, doi: https://doi.org/10.1088/1361-665X/ab80e4.